

**Martensitic Transformation in NiMnGa Single Crystals:
Numerical Simulation and Experiments**

M. Arndt, M. Griebel, V. Novák, P. Šittner, T. Roubíček

no. 223

Diese Arbeit ist mit Unterstützung des von der Deutschen Forschungsgemeinschaft getragenen Sonderforschungsbereiches 611 an der Universität Bonn entstanden und als Manuskript vervielfältigt worden.

Bonn, Mai 2005

Martensitic Transformation in NiMnGa Single Crystals: Numerical Simulation and Experiments

M. Arndt ^{a,*}, M. Griebel ^a, V. Novák ^b, T. Roubíček ^{c,d}, P. Šittner ^b

^a*Institut für Numerische Simulation, Rheinische Friedrich-Wilhelms-Universität Bonn, Wegelerstraße 6, 53115 Bonn, Germany.*

^b*Institute of Physics, Academy of Sciences, Na Slovance 2, CZ-182 21 Praha 8, Czech Republic.*

^c*Faculty of Mathematics and Physics, Charles University, Sokolovská 83, CZ-186 75 Praha 8, Czech Republic.*

^d*Institute of Information Theory and Automation, Academy of Sciences, Pod vodárenskou věží 4, CZ-182 08 Praha 8, Czech Republic.*

Abstract

In this article, we develop a continuum mechanical model to simulate deformation and phase transformation processes in shape memory alloys. The model is based on a detailed description of the stored energy. Furthermore, the energy dissipation due to phase transformations is taken into account via the maximum-dissipation principle. The results from the 3D numerical simulations of stress induced transformations from the cubic to the tetragonal phase and martensitic variant reorientations in NiMnGa are compared with laboratory experiments on NiMnGa [001]-oriented single crystals.

Key words: A. Microstructures, A. Phase transformation, B. Shape memory alloys, C. Mechanical testing, C. Numerical algorithms.

PACS: 64.70Kb.

MSC (2000): 49S05, 74N20, 74S05.

1 Introduction

The functional thermomechanical behavior of shape-memory alloys (SMAs) has been investigated in the past decades from both the experimental and the theoretical viewpoints. SMAs undergo solid-to-solid phase transformations between the

* Corresponding author.

Email address: arndt@ins.uni-bonn.de (M. Arndt).

URL: <http://www.ins.uni-bonn.de> (M. Arndt).

high symmetry austenite phase (typically cubic) and several martensite phases with lower symmetries (i.e. tetragonal, trigonal, orthorhombic or monoclinic) which occur in various variants (mostly 3, 4, 6 or 12). Phase transformations can be induced by temperature and mechanical stress and are typically dissipative. In spite of a very good knowledge of the crystallography, physics and thermodynamics of phase transformations and a vast amount of experimental data available in the literature (see Frémond and Miyazaki (1996)), the prediction of the thermomechanical behavior of SMAs still remains a difficult problem.

Recently, magnetically actuated SMAs such as NiMnGa or CoNiAl have attracted special attention. Experimental results suggest that selected materials, besides their magnetic applications, can be used similarly as superelastic SMAs, see for example Karaca et al. (2003) or Sozinov et al. (2004). They exhibit a narrow stress hysteresis at slightly higher temperatures than superelastic SMAs, even in the polycrystalline state. In this respect, modeling and numerical simulation is of interest. This way, the behavior of fine martensite microstructures in single crystals and the related energy dissipation can be predicted to some extent. The modeling can be approached either on the atomistic level or on various continuum mechanical levels (Pitteri and Zanzotto (2002), Roubíček (2000, 2004)). There are a lot of models for SMAs. Let us name, without any ambitions for completeness, the models of Falk (1980, 1982), Falk and Konopka (1990), Frémond (1987), Frémond and Miyazaki (1996), James (1996), Leclercq et al. (1995), Raniecki et al. (1992), Mielke et al. (2002), Rajagopal and Srinivasa (1998), Kružík and Otto (2004), Mielke and Roubíček (2003), Roubíček (2000) and others. In this article, we use the model proposed in Roubíček (2000), which was further developed theoretically and numerically in Arndt et al. (2003), Plecháč and Roubíček (2002) and Rajagopal and Roubíček (2003).

In this paper, we compare the results of three-dimensional numerical simulations of compression tests on NiMnGa single crystals with the results of laboratory experiments. In Section 2, we discuss how SMAs store and dissipate energy and formulate the mathematical model. Section 3 is devoted to the experiments. First, we describe the laboratory experiments for the cubic to tetragonal martensitic transformation and variant reorientation in a NiMnGa single crystal under compression. Then, we explain the discretization and the numerical solution procedure for this model. Furthermore, the results of both the laboratory experiments and the simulations are discussed and compared to each other. Here, special attention is paid to the stress-strain relation and to the hysteretic behavior. Some concluding remarks are given in Section 4.

2 Mathematical model of phase transformations

In the past two decades, there has been an intensive effort among both, mathematicians and physicists, to describe the multiwell character of the stored energy in SMAs in detail. Often, this was motivated by the belief that the minimum-energy principle governs the steady-state configurations as in conventional small-strain

elasticity. Sometimes, even only the positions of the local minima of the free energy have been examined. Particular contributions to this topic are due to Ball and James (1987, 1992), Bhattacharya (1992, 2004), Bhattacharya et al. (1994), Ericksen (1986, 1987), Müller (1999) and many others, see for instance James and Hane (2000), Luskin (1996) and the references therein. Although the minimum-energy principle is sometimes questionable (Rajagopal and Roubíček (2003)), it qualitatively explains many phenomena which have been observed experimentally in SMA, especially various types of microstructure. Therefore, the detailed description of the stored energy is important and serves as the departure point for the derivation of most mathematical models.

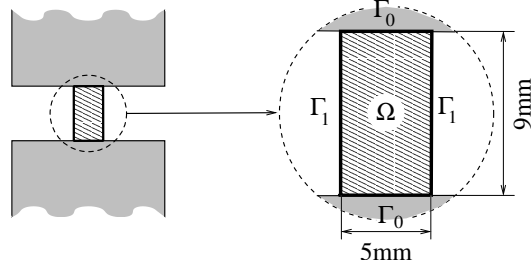


Fig. 1. Hard device loading of a $9 \times 5 \times 5$ mm SMA specimen.

2.1 Stored energy

There is one natural state of the material, namely the parent austenite in the stress-free configuration. We assume that the specimen is suitably fixed in a loading device like in Figure 1. The domain in space it then occupies is called the reference configuration $\Omega \subset \mathbb{R}^3$. The function $y : \Omega \rightarrow \mathbb{R}^3$ denotes the deformation and $u : \Omega \rightarrow \mathbb{R}^3$ the displacement, related by $y(x) = x + u(x)$ for $x \in \Omega$. Hence $\nabla y = \mathbf{I} + \nabla u$, where $\mathbf{I} \in \mathbb{R}^{3 \times 3}$ denotes the identity matrix and ∇ is the Lagrangian gradient operator. The stored energy density $\varphi : \mathbb{R}^{3 \times 3} \rightarrow \mathbb{R}$ in the bulk related to the elastic response is assumed to depend on the deformation gradient F , i.e.

$$\varphi = \varphi(F), \quad F = \nabla y = \mathbf{I} + \nabla u. \quad (1)$$

The Piola-Kirchhoff stress $\sigma_{\text{el}} : \Omega \rightarrow \mathbb{R}^{3 \times 3}$ is then given by

$$\sigma_{\text{el}}(\nabla y) = \varphi'(\nabla y). \quad (2)$$

Let us note that more general energy functions which additionally depend on higher order derivatives have been studied in Arndt and Griebel (2005).

The requirement of frame indifference leads to $\varphi(F) = \varphi(RF)$ for all $R \in \text{SO}(3)$, where $\text{SO}(3)$ denotes the special orthogonal group of orientation-preserving rotations of \mathbb{R}^3 . This requirement makes the specific stored energy φ in fact depend only on the right Cauchy-Green tensor $C = F^\top F$. Besides, φ is subjected to the symmetry relation $\varphi(S^\top F S) = \varphi(F)$ for all matrices S from the symmetry group of the parent austenite.

Let us now explain how the stored energy density ϕ is constructed from experimentally available data. SMA crystals can occur in various stress-free configurations. In the case of a NiMnGa alloy which we are interested in here, there are a cubic *austenite* phase and a lower-symmetrical phase, called *martensite*. The latter is tetragonal and has three variants by symmetry, see Ball and James (1992), Bhattacharya (1992), Bhattacharya et al. (1994) and James and Hane (2000) for a detailed explanation. These stress-free configurations are determined by four distortion matrices F_α , $\alpha = 0, 1, 2, 3$, where $\alpha = 0$ corresponds to the cubic austenite phase and $\alpha = 1, 2, 3$ to the martensitic variants. As the stress-free parent austenite is naturally considered as the reference configuration, we set in view of (1)

$$F_0 = I = \begin{pmatrix} 1 & 0 & 0 \\ 0 & 1 & 0 \\ 0 & 0 & 1 \end{pmatrix}. \quad (3)$$

The other matrices F_1 , F_2 and F_3 refer to the particular variants of the tetragonal martensite and are given by

$$F_1 = \begin{pmatrix} \eta_2 & 0 & 0 \\ 0 & \eta_1 & 0 \\ 0 & 0 & \eta_1 \end{pmatrix}, \quad F_2 = \begin{pmatrix} \eta_1 & 0 & 0 \\ 0 & \eta_2 & 0 \\ 0 & 0 & \eta_1 \end{pmatrix}, \quad F_3 = \begin{pmatrix} \eta_1 & 0 & 0 \\ 0 & \eta_1 & 0 \\ 0 & 0 & \eta_2 \end{pmatrix}. \quad (4)$$

The lattice parameters of the Ni-29.1wt.%Mn-21.2wt.%Ga alloy considered here are $a_0 = 0.5839\text{nm}$ for the cubic austenite at temperature $T = 323\text{K}$ and $a_M = b_M = 0.5945\text{nm}$ and $c_M = 0.5610\text{nm}$ for the martensite at temperature $T = 293\text{K}$, see Straka et al. (2004). Therefore we have $\eta_1 = a_M/a_0 \approx 1.018$ and $\eta_2 = c_M/a_0 \approx 0.961$ in (4).

The free energy Ψ_0 of the austenite has the form

$$\Psi_0(F, T) = \hat{\phi}_0(\varepsilon) - c_A T \ln(T), \quad \varepsilon = \frac{1}{2}(F^\top F - I), \quad (5)$$

where T denotes the temperature and ε the Green strain tensor. The constant c_A denotes the heat capacity of the austenite and $\hat{\phi}_0$ the specific stored energy. Following Ericksen (1986, 1987), the latter is given in the form of an anisotropic St. Venant-Kirchhoff material, i.e. in the cubic case by

$$\hat{\phi}_0(\varepsilon) = \frac{\mathbb{C}_{11}}{2}(\varepsilon_{11}^2 + \varepsilon_{22}^2 + \varepsilon_{33}^2) + \mathbb{C}_{12}(\varepsilon_{11}\varepsilon_{22} + \varepsilon_{11}\varepsilon_{33} + \varepsilon_{22}\varepsilon_{33}) \\ + 2\mathbb{C}_{44}(\varepsilon_{12}^2 + \varepsilon_{13}^2 + \varepsilon_{23}^2). \quad (6)$$

For the elastic moduli \mathbb{C} we use the standard Voigt notation. According to Mañosa et al. (1997), the concrete values are given by $\mathbb{C}_{11} = 136\text{GPa}$, $\mathbb{C}_{12} = 92\text{GPa}$ and $\mathbb{C}_{44} = 102\text{GPa}$. Note however that values measured in laboratory experiments are

considerably lower due to the softness of the testing machine, sample shape effects, and namely due to the uncertainty arising from precursor phenomena upon stressing at temperatures near the transition temperature. Since these phenomena in NiMnGa are not well understood yet, they cannot be considered in the modeling. To compensate for this, we scaled the elastic constants so that experimental and theoretical moduli coincide. Note that the numerical experiments shown below nevertheless correctly reproduce the elastic moduli as they are set up in the model.

Let us note that the quadratic form (6) gives the Cauchy stress $\sigma = \hat{\phi}'_0(\varepsilon)$, i.e.

$$\begin{pmatrix} \sigma_{11} \\ \sigma_{22} \\ \sigma_{33} \\ \sigma_{23} \\ \sigma_{13} \\ \sigma_{12} \end{pmatrix} = \begin{pmatrix} \mathbb{C}_{11} & \mathbb{C}_{12} & \mathbb{C}_{12} & 0 & 0 & 0 \\ \mathbb{C}_{12} & \mathbb{C}_{11} & \mathbb{C}_{12} & 0 & 0 & 0 \\ \mathbb{C}_{12} & \mathbb{C}_{12} & \mathbb{C}_{11} & 0 & 0 & 0 \\ 0 & 0 & 0 & 4\mathbb{C}_{44} & 0 & 0 \\ 0 & 0 & 0 & 0 & 4\mathbb{C}_{44} & 0 \\ 0 & 0 & 0 & 0 & 0 & 4\mathbb{C}_{44} \end{pmatrix} \begin{pmatrix} \varepsilon_{11} \\ \varepsilon_{22} \\ \varepsilon_{33} \\ \varepsilon_{23} \\ \varepsilon_{13} \\ \varepsilon_{12} \end{pmatrix}, \quad (7)$$

when we take $\sigma_{ij} = \sigma_{ji}$ into account. Obviously we have $\hat{\phi}_0(\varepsilon) = \frac{1}{2} \sum_{i,j=1}^3 \sigma_{ij} \varepsilon_{ij}$.

For each particular martensitic variant, the strain must refer to the corresponding stress-free configuration rather than to the cubic austenite. This means we replace the strain tensor by $\varepsilon = \frac{1}{2}(F_\alpha^{-\top} F^\top F F_\alpha^{-1} - I)$. The free energy of the martensitic variant is then given by

$$\Psi_\alpha(F, T) = \hat{\phi}_\alpha \left(\frac{F_\alpha^{-\top} F^\top F F_\alpha^{-1} - I}{2} \right) - c_M T \ln(T) + c_0, \quad \alpha = 1, 2, 3, \quad (8)$$

where c_M is the heat capacity of the martensite and c_0 is an offset. In general we have $c_A > c_M > 0$ due to the shape memory effect which energetically prefers the austenite phase for higher temperatures. For the quadratic form $\hat{\phi}_\alpha$ we use the expression (6) from the austenite due to the lack of experimental data for the martensitic moduli.

As usual in statistical physics, the overall specific free energy $\Psi(F, T)$ can be taken as the thermal average

$$\Psi(F, T) = -k_B T \ln \left(\sum_{\alpha=0}^3 e^{-\frac{\Psi_\alpha(F, T)}{k_B T}} \right) \quad (9)$$

where k_B is the Boltzmann constant per unit volume and T is the temperature. However, we use two simplifications. First, the formula (9) is nearly identical to the minimum

$$\Psi(F, T) = \min_{\alpha=0, \dots, 3} (\Psi_\alpha(F, T)) \quad (10)$$

of the free energies Ψ_α , as the wells F_α are sufficiently distant from each other.

Second, we linearize the overall offset of martensite against austenite by approximating

$$\Psi_0(I, T) - \Psi_\alpha(F_\alpha, T) \approx C(T - T_{\text{eq}}) =: \psi_\alpha(T), \quad \alpha = 1, 2, 3 \quad (11)$$

around the so-called equilibrium temperature T_{eq} . The equilibrium temperature T_{eq} is the temperature for which all wells have equal energy, i.e. $\Psi_0(I, T_{\text{eq}}) = \Psi_\alpha(F_\alpha, T_{\text{eq}})$. Thus T_{eq} is determined by $(c_M - c_A)T_{\text{eq}} \ln(T_{\text{eq}}) = c_0$. Physical experiments show that the martensite phase in an unloaded NiMnGa specimen starts to appear upon cooling at the martensite start temperature $M_s = 308$ K and disappears upon heating at the austenite finish temperature $A_f = 317$ K, see Straka et al. (2004). Thus we may assume that both phases are in equilibrium at the temperature $T_{\text{eq}} = 313$ K. The constant C is the Clausius-Clapeyron slope multiplied by the transformation strain, here about 6%. From Straka et al. (2004) we also know that the Clausius-Clapeyron slope is 3 MPa/K, which gives us $C = 3 \text{ MPa/K} \cdot 6\% = 180 \text{ kPa/K}$.

Setting $\psi_0 = 0$, the linearization leads to

$$\Psi(F, T) = \min_{\alpha=0, \dots, 3} \left(\hat{\phi}_\alpha \left(\frac{F_\alpha^{-\top} F^\top F F_\alpha^{-1} - I}{2} \right) + \psi_\alpha(T) \right) - c_A T \ln(T). \quad (12)$$

The term $c_A T \ln(T)$ is neglected since an additive parameter is not relevant for the potential here. We treat the temperature T as a fixed parameter and finally obtain the stored energy

$$\varphi(F) = \min_{\alpha=0, \dots, 3} \left(\hat{\phi}_\alpha \left(\frac{F_\alpha^{-\top} F^\top F F_\alpha^{-1} - I}{2} \right) + \psi_\alpha(T) \right). \quad (13)$$

Both options (9) and (13) exhibit the same multiwell character: the energies have four local minima in the form of orbits. In (13), these orbits are precisely the desired deformation gradients $\text{SO}(3)F_\alpha$ of the particular phase variants $\alpha = 0, \dots, 3$. Besides, (13) is much faster to evaluate numerically than (9). Therefore we use it in our model. This accelerates the calculations considerably since φ and its derivatives must be evaluated many times (typically around 10^{11} times) within the numerical simulations presented below.

The overall elastic energy V_{el} is now given by

$$V_{\text{el}}(y) = \int_{\Omega} \varphi(\nabla y) \, dx. \quad (14)$$

Beside the above contribution to the stored energy from the deformation gradient, often higher-order terms are added to reflect the interfacial energies. Standard interfacial energies are given by

$$V_{\text{if}}(y) = \int_{\Omega} |\nabla^2 y|^2 \, dx \quad \text{or} \quad V_{\text{if}}(y) = \int_{\Omega} |\Delta y|^2 \, dx, \quad (15)$$

see Abeyaratne and Knowles (1992). They contribute to the stress tensor by the term $-\nabla\Delta y$ or $-\Delta\nabla y$, respectively. This causes the interfaces to be diffuse rather than sharp, which contradicts experimental evidence that interfaces observed in SMA are often close to being atomically sharp, see Ren and Truskinovsky (2000). As a remedy, a nonlocal energy of the form

$$V_{\text{if}}(y) = \frac{1}{4} \int_{\Omega} \int_{\Omega} K(x, \tilde{x}) |\nabla y(x) - \nabla y(\tilde{x})|_{\mathbb{F}}^2 dx d\tilde{x} \quad (16)$$

with a suitable kernel K (see Rogers and Truskinovsky (1997)) can be used, where $|F|_{\mathbb{F}} = (\sum_{ij} F_{ij}^2)^{1/2}$ denotes the Frobenius norm of a matrix F . The interfacial energy (16) contributes to the overall stress tensor by

$$\sigma_{\text{if}}(\nabla y) = \nabla y(x) \int_{\Omega} K(x, \tilde{x}) d\tilde{x} - \int_{\Omega} K(x, \tilde{x}) \nabla y(\tilde{x}) d\tilde{x}. \quad (17)$$

For kernels $K(x, \tilde{x}) = |x - \tilde{x}|^{-3-2\gamma}$ with $0 < \gamma < \frac{1}{2}$, this approach allows for sharp interfaces as shown in Arndt et al. (2003). Note furthermore that (16) is frame indifferent in contrast to the interfacial energies (15).

2.2 Dissipation energy

The dynamics of martensitic phase transformations is a complicated and still not fully understood process. There are intensive investigations based on the hypothesis that the interface between various martensitic variants or between the austenitic phase and particular martensitic variants moves as a whole two-dimensional interface. It is assumed that its dynamics can basically be read off from the shape of the stored energy, see Abeyaratne and Knowles (1992) or Truskinovsky (1994) and the references cited therein. However, this does not seem to be relevant to phase transformations in SMAs where the movement of one-dimensional singularities or dislocations can be activated by much lower energies than the whole two-dimensional interface. On the continuum mechanical level, this process can only be modeled phenomenologically up to now. One possibility was suggested by Abeyaratne and Vedantam (1999), which results in a non-specified interface propagation speed.

Here we follow this approach to capture the energetics correctly to a good extent. We rely on the hypothesis that this determines the macroscopical response of SMAs. To be more specific, the hypothesis for our model is that each particular phase transformation dissipates a specific amount of energy, independently of the way and the speed of the transformation process. This reflects the experimental observation that the hysteretic behavior of the stress-strain response is rate-independent except for very fast loadings. Nevertheless this hypothesis is slightly simplifying because a certain rate dependency inevitably comes from the intimate coupling with the temperature field and possibly from other effects like the extra dissipation in shock waves with supersonic speed (Abeyaratne and Knowles (1992), Truskinovsky (1994)), inertial forces and viscous-like damping.

To incorporate the energy which corresponds to particular phase transforma-

tions, we must distinguish the particular phases and phase variants. To this end, we introduce a function

$$\lambda = \lambda(F) = (\lambda_0(F), \dots, \lambda_3(F)) : \mathbb{R}^{3 \times 3} \rightarrow [0, 1]^4 \quad (18)$$

which plays the role of a multidimensional order parameter. It is constructed to be frame indifferent, i.e. $\lambda(F) = \lambda(RF)$ for any $R \in \text{SO}(3)$. Each λ_α equals one in a neighborhood of the well $\text{SO}(3)F_\alpha$ and vanishes far away from it, in particular in the neighborhood of the remaining wells $\text{SO}(3)F_\beta$ with $\beta \neq \alpha$. The behavior of λ in the spinodal region, i.e. away from all wells, does not seem to be important as the deformation gradients mostly live in a rather close neighborhood of the wells. Thus the overall energetics does not depend much on the modeling of the energy in this region. Furthermore, we assume λ to be differentiable for technical reasons, see Arndt et al. (2003) for more details. A similar construction which additionally satisfies $\sum_{\alpha=0}^3 \lambda_\alpha = 1$ has been proposed in Mielke and Theil (1999), Mielke et al. (2002) and was further used in Govindjee et al. (2003) and Mielke and Roubíček (2003).

Finally, we use Hill's maximum-dissipation principle (see Hill (1948)) as given in (25) below to make the dissipation of energy due to phase transformations rate-independent like in conventional plasticity. The essential point is to postulate a dissipation potential $\xi : \mathbb{R}^4 \rightarrow \mathbb{R}$ which is convex, non-negative and positive homogeneous. Let us remark that its subdifferential

$$\partial\xi : \mathbb{R}^4 \rightrightarrows \mathbb{R}^4, \quad \partial\xi(z) = \{z^* \in \mathbb{R}^4; \forall \tilde{z} \in \mathbb{R}^4 : z^* \cdot (z - \tilde{z}) + \xi(\tilde{z}) \geq \xi(z)\} \quad (19)$$

is then so-called maximally responsive, see Eve et al. (1990). Here we use

$$\xi(z) = \sum_{\alpha=0}^3 \mathcal{E}_\alpha |z_\alpha|, \quad (20)$$

where the constants $\mathcal{E}_\alpha \geq 0$ reflect the energy which is dissipated when the volume fraction of the corresponding phase changes from 0% to 100% or vice versa. Because of the symmetry of the martensitic variants, we naturally have $\mathcal{E}_1 = \mathcal{E}_2 = \mathcal{E}_3$. Hence we must set up the two parameters \mathcal{E}_0 and \mathcal{E}_1 which satisfy

$$\begin{aligned} \mathcal{E}_0 + \mathcal{E}_1 &= \text{specific energy dissipated during the A/M or M/A transformation,} \\ 2\mathcal{E}_1 &= \text{specific energy dissipated during the M/M transformation,} \\ &\text{i.e. reorientation of martensite.} \end{aligned} \quad (21)$$

The values for \mathcal{E}_0 and \mathcal{E}_1 will be determined from measurements in Section 3.1. Let us remark that a nonsymmetric function ξ instead of (20) would allow us to distinguish between the energy dissipated during the A/M and the M/A transformation. However, these values are not experimentally available, hence we stick to the symmetric definition (20).

The quantity $\xi\left(\frac{\partial}{\partial t}\lambda(\nabla y)\right)$ describes the specific dissipation rate. Thus the specific energy which is dissipated during all phase transformation processes over

some time interval $[0, t]$ is given by the total variation

$$\xi \left(\text{Var}_{[0,t]} \lambda(\nabla y(x, \cdot)) \right) = \sum_{\alpha=0}^3 \mathcal{E}_\alpha \text{Var}_{[0,t]} \lambda_\alpha(\nabla y(x, \cdot)). \quad (22)$$

Let us remind that the total variation $\text{Var}_{[0,t]} \lambda_\alpha(\nabla y(x, \cdot))$ for a differentiable function $t \mapsto \lambda_\alpha(\nabla y(x, t))$ is just equal to $\int_0^t \left| \frac{\partial}{\partial t} \lambda_\alpha(\nabla y(x, \tau)) \right| d\tau$. The formula (22) counts, roughly speaking, how many times a phase transformation happened at a current point $x \in \Omega$, independently of its speed.

The stress which is related to the dissipative mechanism (22) and which we therefore call the (quasi)plastic stress is given by

$$\sigma_{\text{pl}} \left(\nabla y, \frac{\partial}{\partial t} \nabla y \right) = \omega \cdot \lambda'(\nabla y) \quad (23)$$

with

$$\omega \in \partial \xi \left(\frac{\partial}{\partial t} \lambda(\nabla y) \right) = \partial \xi \left(\lambda'(\nabla y) : \frac{\partial}{\partial t} \nabla y \right), \quad (24)$$

where $\partial \xi$ is defined by (19) and “:” denotes the scalar product of matrices. Particular components of the vector $\omega = \omega(x, t) \in \mathbb{R}^4$ represent specific energies (or “pressures”) which drive the respective phase transformation, provided their magnitudes achieve the activation thresholds \mathcal{E}_α from (20). In particular, the inclusion in (24) yields

$$\frac{\partial}{\partial t} \lambda(\nabla y) \cdot \omega = \max_{z \in \partial \xi(0)} \frac{\partial}{\partial t} \lambda(\nabla y) \cdot z, \quad (25)$$

see Eve et al. (1990) for detailed mathematical arguments. This resembles Hill’s maximum-dissipation principle which says that the driving energies $\omega = (\omega_0, \dots, \omega_3)$ make the dissipation of the phase transformation maximal among all admissible driving energies $\partial \xi(0) = \prod_{\alpha=0}^3 [-\mathcal{E}_\alpha, \mathcal{E}_\alpha]$ for the considered volume-fraction rate $\frac{\partial}{\partial t} \lambda(\nabla y)$. An alternative way to express the same principle like in plasticity theory is that the rate of plastic deformation belongs to the cone of outward normals of the elasticity domain. In our context, it means that the rate $\frac{\partial}{\partial t} \lambda(\nabla y)$ of phase transformations belongs to the normal cone of the “elasticity domain” $\partial \xi(0)$ at the point ω . In particular, (25) says that $\frac{\partial}{\partial t} \lambda(\nabla y) = 0$ if ω is inside $\partial \xi(0)$, i.e. the volume fractions do not change if there is not enough driving stress to activate the transformation.

Moreover, it is reasonable to augment the interfacial stored energy (16) by its respective viscous mechanism $V_{\text{if}}(\frac{\partial}{\partial t} y)$, especially for the analysis. This reflects the general experience that no physical mechanism can store energy with 100% efficiency, i.e. without any dissipation. The viscous stress is then given by $\sigma_{\text{if}}(\frac{\partial \nabla y}{\partial t})$. Let us note that a viscous mechanism of this form obeys the law of frame indifference, in contrast to other standard viscous terms like $|\Delta y_t|^2$ or $|\nabla^2 y_t|^2$, see Antman (1998) for a detailed discussion.

2.3 Mathematical model and energy balance

We model the phase transformation on the basis of the stored energy and the dissipative mechanisms described in Sections 2.1 and 2.2, respectively. This leads to the evolution equation

$$\rho \frac{\partial^2 y}{\partial t^2} - \operatorname{div} \left(\sigma_{\text{el}}(\nabla y) + \sigma_{\text{pl}} \left(\nabla y, \frac{\partial \nabla y}{\partial t} \right) + \sigma_{\text{if}} \left(\mu \nabla y + \nu \frac{\partial}{\partial t} \nabla y \right) \right) = 0, \quad (26)$$

where σ_{el} stems from (2), σ_{pl} from (23) and σ_{if} from (17). The constants $\mu \geq 0$ and $\nu \geq 0$ denote the ‘‘capillarity’’ and ‘‘viscosity’’ coefficients. We neglect the gravity body forces by setting the right hand side in (26) to zero, which is reasonable since they are smaller by several orders of magnitude than the elastic and plastic forces. Because of (24), the system (26) represents rather a differential inclusion than an equation.

We prescribe the initial conditions for the deformation $y(x, 0) = y_0(x)$ at the starting time $t = 0$ as well as the velocity $\frac{\partial y}{\partial t}(x, 0) = v_0(x)$. The precise initial deformation depends on the respective experiment and will be given in Section 3.2. The initial velocity $v_0(x)$ is set to zero to express that the specimen is originally in a non-moving state. Moreover, (26) has to be completed by suitable boundary conditions. In view of the typical arrangement of laboratory experiments, we consider hard-device loading which acts on the part Γ_0 of the boundary $\partial\Omega$ of the specimen Ω as indicated in Figure 1. This type of loading can be incorporated by Dirichlet boundary conditions $y(x, t) = y_D(x, t)$ for $x \in \Gamma_0$. The remaining part $\Gamma_1 = \partial\Omega \setminus \Gamma_0$ of the boundary is stress free, i.e. the normal stress

$$\left(\sigma_{\text{el}}(\nabla y) + \sigma_{\text{pl}} \left(\nabla y, \frac{\partial \nabla y}{\partial t} \right) + \sigma_{\text{if}} \left(\mu \nabla y + \nu \frac{\partial \nabla y}{\partial t} \right) \right) \vec{n} \quad (27)$$

vanishes. Here $\vec{n} = \vec{n}(x)$ denotes the normal vector to Γ_1 .

An important justification of the model is the energy balance of the process over some time interval $[0, t]$. It can be obtained by multiplying (26) with the velocity $\frac{\partial y}{\partial t}$, using Green’s formula in space and integrating over the space Ω and the time interval $(0, t)$. This gives

$$\underbrace{E \left(y(t), \frac{\partial y}{\partial t}(t) \right)}_{\substack{\text{total energy} \\ \text{at time } t}} + \underbrace{\int_0^t R \left(y(\tau), \frac{\partial y}{\partial t}(\tau) \right) d\tau}_{\substack{\text{dissipated} \\ \text{energy}}} = \underbrace{E(y_0, v_0)}_{\substack{\text{total energy} \\ \text{at time } 0}} + \underbrace{\int_0^t \int_{\Gamma_0} \sigma_n \cdot \frac{\partial y}{\partial t} dS}_{\substack{\text{work of} \\ \text{external forces}}} d\tau \quad (28)$$

where σ_n is the normal stress on the part Γ_0 of the boundary $\partial\Omega$ with prescribed deformation, see Arndt et al. (2003) for more details concerning σ_n . The total energy

E in (28) involves the kinetic energy and all stored energies:

$$\begin{aligned} E(y, v) &= V_{\text{kin}}(v) + V_{\text{el}}(y) + \mu V_{\text{if}}(\nabla y) \\ &= \int_{\Omega} \left(\frac{\rho}{2} |v|^2 + \varphi(\nabla y) + \frac{1}{4} \mu \int_{\Omega} K(x, \tilde{x}) |\nabla y(x) - \nabla y(\tilde{x})|_{\mathbb{F}}^2 d\tilde{x} \right) dx. \end{aligned} \quad (29)$$

R is the dissipation rate over the volume Ω . It is given implicitly by

$$\int_0^t R \left(y(\tau), \frac{\partial y}{\partial t}(\tau) \right) d\tau = \int_{\Omega} \xi \left(\text{Var}_{[0,t]} \lambda(\nabla y(x, \cdot)) \right) dx + 2\nu \int_0^t V_{\text{if}} \left(\frac{\partial}{\partial t} \nabla y \right) dt. \quad (30)$$

If the deformation function y is smooth, R can be written as

$$R(y, v) = \int_{\Omega} \xi(\lambda(\nabla y) : \nabla v) dx + 2\nu V_{\text{if}}(\nabla v). \quad (31)$$

The important trick to obtain the term $\xi(\text{Var}_{[0,t]} \lambda(\nabla y(x, \cdot)))$ from (26) is the formula

$$\sigma_{\text{pl}} \left(\nabla y, \frac{\partial \nabla y}{\partial t} \right) : \frac{\partial \nabla y}{\partial t} = \omega \cdot \lambda'(\nabla y) : \frac{\partial \nabla y}{\partial t} = \omega \cdot \frac{\partial}{\partial t} \lambda(\nabla y) = \sum_{\alpha=0}^3 \mathcal{E}_{\alpha} \left| \frac{\partial}{\partial t} \lambda_{\alpha}(\nabla y) \right| \quad (32)$$

which holds for any choice of ω satisfying (24). Of course, the energy dissipated during the phase transformation is eventually transformed to heat because there are no permanent structural changes in SMAs. We assume that the process is sufficiently slow so that the created heat is lead off and the specimen is kept at constant temperature.

In case of $\nu > 0$, the energy balance (28) can be proved thanks to the presence of the viscous-like term $\text{div} \left(\sigma_{\text{if}} \left(\nu \frac{\partial \nabla y}{\partial t} \right) \right)$ in (26), see Arndt et al. (2003) and Plecháč and Roubíček (2002). This term regularizes and prevents the development of shock waves which might dissipate additional energy. Otherwise (28) only holds as an inequality, see Abeyaratne and Knowles (1992) or Truskinovsky (1994).

3 Compression experiments with NiMnGa single crystals

In this section, we discuss our experimental and numerical compression experiments for a NiMnGa alloy and compare their results.

3.1 Laboratory experiments

The specimens consist of Ni-29.1wt.%Mn-21.2wt.%Ga single crystals grown by a modified Bridgman method by AdaptaMat Ltd., Finland. They have been cut in the martensite state as cuboids with dimensions $4 \times 4 \times 10$ mm and edges parallel to the [100], [010] and [001] directions. In the unstressed austenite state, they are slightly irregular with dimensions $9 \times 5 \times 5$ mm. Since the transformation to the five-layered modulated tetragonal 5M martensite occurs at $M_s = 308$ K and the reverse

transformation to the cubic phase occurs at $A_f = 317$ K, the specimen exists at room temperature in the martensite phase.

The specimen was deformed by compression at the temperatures 293 K and 323 K in a Tiratest 2300 testing machine which is equipped with a hot air temperature chamber, see Figure 1 for a schematic diagram. At $T = 323$ K, the loading started from the austenite state. In order to obtain a defined material state in the reorientation experiments which start from the martensite state at $T = 293$ K, the specimen was subsequently compressed up to 60 MPa along all three crystal directions [100], [010] and [001]. As a consequence, the specimen mostly consisted of one martensitic variant with the c-axis ([001] martensite direction) oriented along the last direction of stressing. The specimen was placed into the deformation machine with the c-axis perpendicular to the load axis and deformed by compression at the selected temperature. More details for the experimental setup can be found in Straka et al. (2004).

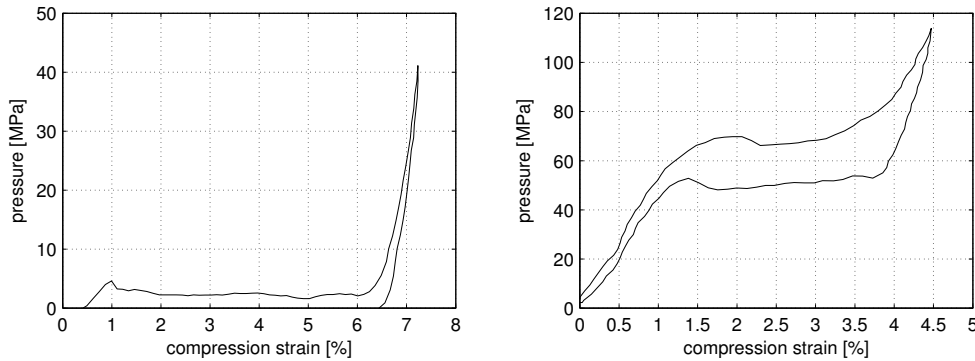


Fig. 2. Stress-strain diagram of the laboratory experiments at $T = 293$ K (left) and $T = 323$ K (right).

The stress-strain curves measured at $T = 293$ K and $T = 323$ K are shown in Figure 2. The martensite reorientation at $T = 293$ K proceeds with a very small stress of 2–4 MPa and yields almost 6% of strain unrecovered upon unloading. In spite of the large strain, the stored elastic energy and the dissipated energy are very small. At $T = 323$ K, the specimen shows the typical pseudoelastic response with a stress-induced cubic-to-tetragonal transformation at a transformation stress of 50–70 MPa. It yields approximately 2.5% of compression strain recovered upon unloading and a larger hysteresis width of about 20 MPa. Clearly the amounts of stored and dissipated energy are much larger in the latter case.

The changes of microstructure during the variant reorientation process at $T = 293$ K are shown in Figure 3 as a sequence of surface photographs taken during the compression experiment. The reorientation proceeds by a lateral motion of planar interfaces which appear as lines on the surface. One martensitic variant (bright) is switched into another martensitic variant (dark). During the transition process, the specimen exhibits a mixture of both phases in form of a laminated microstructure.

The laboratory measurements also allow us to determine the values for the model parameters \mathcal{E}_0 and \mathcal{E}_1 in Section 2.2. The dissipation energy per unit volume for the austenite-martensite transformation and the backward martensite-austenite

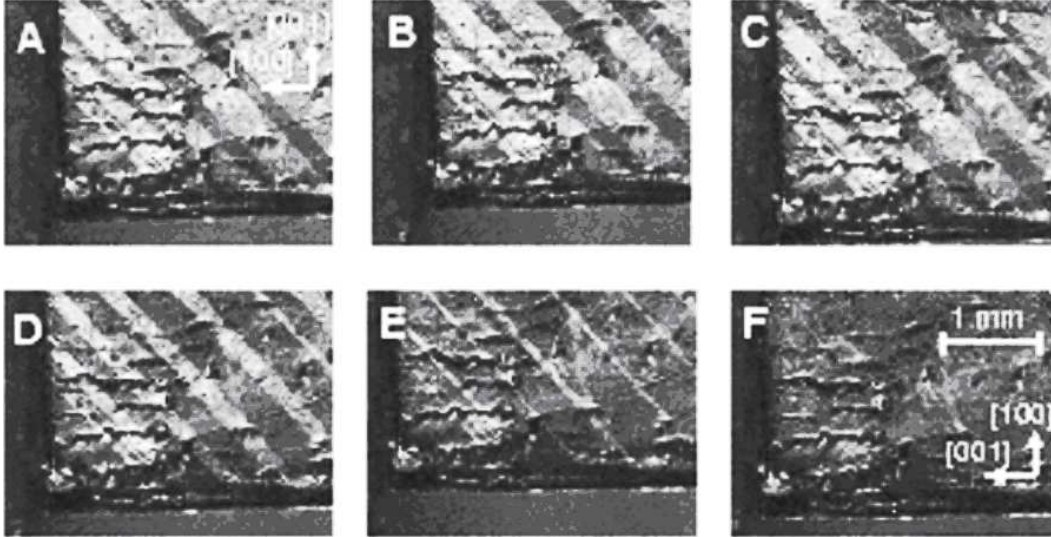


Fig. 3. Evolving microstructure in the laboratory experiment at $T = 293\text{K}$. The photographs show the (010) plane of the crystal. (The photographs are taken from Straka et al. (2004).)

transformation is the area enclosed by the hysteresis loop of the stress-strain diagram in Figure 2 (right). By numerical integration we obtain the value 668 kPa for the area of hysteresis. In view of (21) we conclude $2(\mathcal{E}_0 + \mathcal{E}_1) = 668\text{ kPa}$. Concerning the martensite-martensite transformation (left graph), the measurements only provide the transition from one martensitic phase to another martensitic phase, whereas the backward transformation has not been performed. Consequently the loop in the graph is not closed. But due to symmetry, we can assume that the backward transformation proceeds similarly to the forward transformation, only with negative sign of the stress values. Thus twice the M/M dissipation energy equals twice the area between the stress curve and the horizontal axis. The latter is determined to be 192 kPa. According to (21), we therefore have $4\mathcal{E}_1 = 2 \cdot 192\text{ kPa}$. Altogether, we conclude

$$\mathcal{E}_0 = 238\text{ kPa} \quad \text{and} \quad \mathcal{E}_1 = 96\text{ kPa}. \quad (33)$$

3.2 Numerical simulations

Now we come to the numerical simulation. Let us mention that comparable numerical simulations for a mesoscopical model of NiMnGa alloys which involves Young measures are given in Kružík and Roubíček (2004) and Roubíček and Kružík (2005). Then, three-dimensional simulations similar to ours also have been performed by Klouček and Luskin (1994). They focus on the dynamics of the martensite/austenite interface, but do not take quasi-plastic terms into account. Here, we employ the model described in Section 2. Since the kinetic energy does not play a substantial role due to the relatively slow transformation process, we neglect it here by setting the mass density ρ to zero.

The model is discretized in space with finite elements on a tetragonal grid. To this end, the rectangular domain Ω is uniformly decomposed into 16^3 cuboids,

each of which is subsequently subdivided into 6 tetrahedra. This results in an overall uniform mesh of 24576 tetrahedra. The ansatz space are the P1 Lagrange finite elements, which consist of all functions which are piecewise linear on each tetrahedron, continuous on the whole domain Ω and fulfill the boundary conditions:

$$\mathcal{V}_{\mathcal{T},t} = \{y \in C(\overline{\Omega}; \mathbb{R}^3) : y|_T \text{ is linear } \forall T \in \mathcal{T}, \quad y(x) = y_D(x,t) \forall x \in \Gamma_0\}. \quad (34)$$

Here \mathcal{T} denotes the set of tetrahedra.

The time discretization is done by finite differences. The time interval under consideration is subdivided into time steps t_j , $j = 0, 1, 2, \dots, j_{\max}$. The solution function at the time step j is denoted by $y^{(j)}$. We then reformulate our problem as an incremental energy minimization problem:

$$\begin{aligned} \text{For all } j = 1, 2, 3, \dots, j_{\max} \text{ find } y^{(j)} \in \mathcal{V}_{\mathcal{T},t_j} \text{ which minimizes the energy} \\ V(y^{(j)}) = V_{\text{el}}(y^{(j)}) + \mu V_{\text{if}}(y^{(j)}) + \xi \left(\lambda(\nabla y^{(j)}) - \lambda(\nabla y^{(j-1)}) \right) \\ + \bar{\nu} V_{\text{if}}(y^{(j)} - y^{(j-1)}). \end{aligned} \quad (35)$$

Each minimizer is now a solution of the discretized version of (26). This results in an implicit Euler scheme which involves a nonconvex minimization problem at each time step.

Since it is practically impossible to find a global minimum within the highly nonconvex energy landscape, we employ a local minimization algorithm to find at least a good local minimum. At each time step j , we use the solution $y^{(j-1)}$ of the previous time step as a starting value. After applying the new boundary conditions (recall that they are time dependent) and after adding a small random perturbation, we perform several one-dimensional minimization steps in the direction of steepest descent. The solution is then assigned to $y^{(j)}$. This technique is known as the gradient method. The step size of this line search algorithm is determined by a modified Armijo method. Let us note that more elaborate schemes like variants of the conjugate gradient method have not proven successful in this context due to the highly oscillating second derivative of the energy functional, see Arndt et al. (2003).

Since the local minimum obtained in this way is usually not a global minimum, the procedure induces a certain amount of numerical dissipation. Therefore we additionally use the simulated annealing technique (see Salamon et al. (2002)) to improve the minimization algorithm. This significantly reduces the numerical dissipation.

The simulated annealing technique works as follows. At each time step j , a new deformation function \tilde{y} is generated first by adding a small random displacement to the deformation function $y^{(j)}$ given by the minimization routine above. Second, the energy $V(\tilde{y})$ is computed. If it is lower than the original energy $V(y^{(j)})$, the new deformation is accepted unconditionally, i.e. we redefine $y^{(j)}$ as \tilde{y} . Otherwise, it is accepted with probability $\exp\left(\frac{V(y^{(j)}) - V(\tilde{y})}{k}\right)$. Here k is a fixed parameter which denotes the annealing temperature. Third, the local minimization routine as described above is applied to the newly obtained state. The whole procedure is repeated sev-

eral times.

Further details of the numerical techniques and the supporting analysis including a convergence proof can be found in Arndt et al. (2003) and Plecháč and Roubíček (2002).

We have performed two numerical experiments which resemble the laboratory experiments described in Section 3.1. For the first experiment at $T = 293$ K, the initial conditions as introduced in Section 2.3 are given by $y_0(x) = F_2x$, where the deformation matrix F_2 is defined by (4). The initial deformation corresponds to the martensitic variant of which the specimen in the laboratory experiment consisted at the starting time. For the second experiment at $T = 323$ K, we set $y_0(x) = x$ to mimic the austenite state. In both experiments, we use the initial velocity $v_0(x) = 0$. The constants for the dissipative mechanism as described in Section 2.2 are given by (33).

In contrast to the laboratory experiments, the specimen can now be loaded not only by compression, but also by tension. In the two numerical experiments below, the specimen has been loaded by compression, then unloaded, then loaded by tension and finally unloaded again.

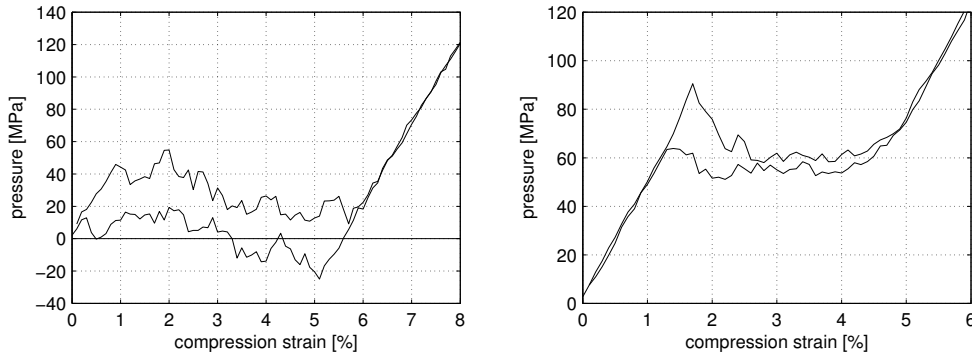


Fig. 4. Numerical simulation of the compression experiments: stress-strain diagram for $T = 293$ K (left) and $T = 323$ K (right).

The stress-strain diagrams for the compression part of our simulations are given in Figure 4. For the experiment with $T = 293$ K (left graph of the figure), the diagram shows a range from 0% to 6% compression strain where the M/M reorientation takes place and where the transformation stress is relatively low. The height of the hysteresis loop is controlled by the parameters \mathcal{E}_0 and \mathcal{E}_1 of the dissipative mechanism, see (33). Outside this transformation zone, the crystal shows a perfectly elastic response without any dissipation. This behavior is in good correspondence with the laboratory experiment.

In the experiment with $T = 323$ K, the pure austenite phase is active in the beginning. The elastic behavior without any dissipation results in a straight line from 0% to 1.5% compression strain in the stress-strain diagram (right graph of Figure 4). Then, the A/M phase transformations with the typical hysteresis loop sets in at 1.5% and lasts to 5%. The stress-strain diagram shows a distinct increase of the stress at the beginning of the phase transformation, before the stress falls down to the roughly flat region. Note that this nucleation peak is not a finite size effect

of the discretization or a consequence of some failure of the numerical algorithm, but is intrinsic to the transformation itself, see Truskinovsky and Vainchtein (2004) for a detailed analysis. In a less distinct way, this peak can be observed in the laboratory experiments as well, see Figure 2. Altogether, the stress-strain behavior in this numerical experiment is also in relatively good correspondence with the laboratory experiment.

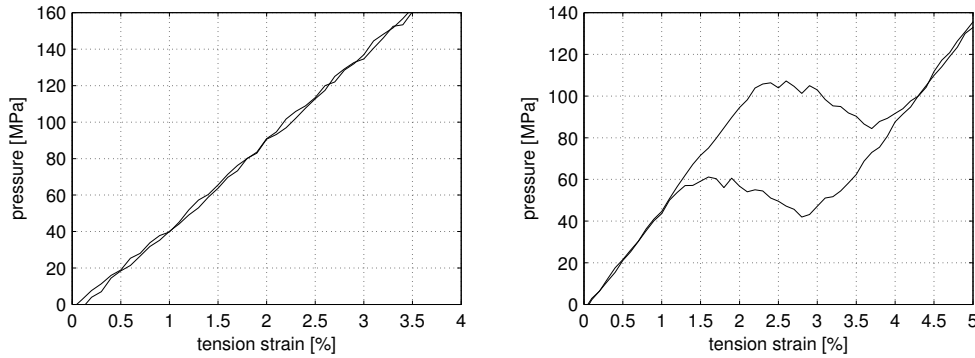


Fig. 5. Numerical simulation of the tension experiments: stress-strain diagram for the temperatures $T = 293$ K (left) and $T = 323$ K (right).

Figure 5 shows the stress-strain diagrams under tension. For the case $T = 293$ K (left graph of the figure), one can clearly observe the linear elastic behavior of the single martensitic variant without any dissipation. For the case $T = 323$ K (right graph of the figure), a transformation from the austenite to a mixture of two martensitic variants occurs, which is accompanied by a certain hysteresis.

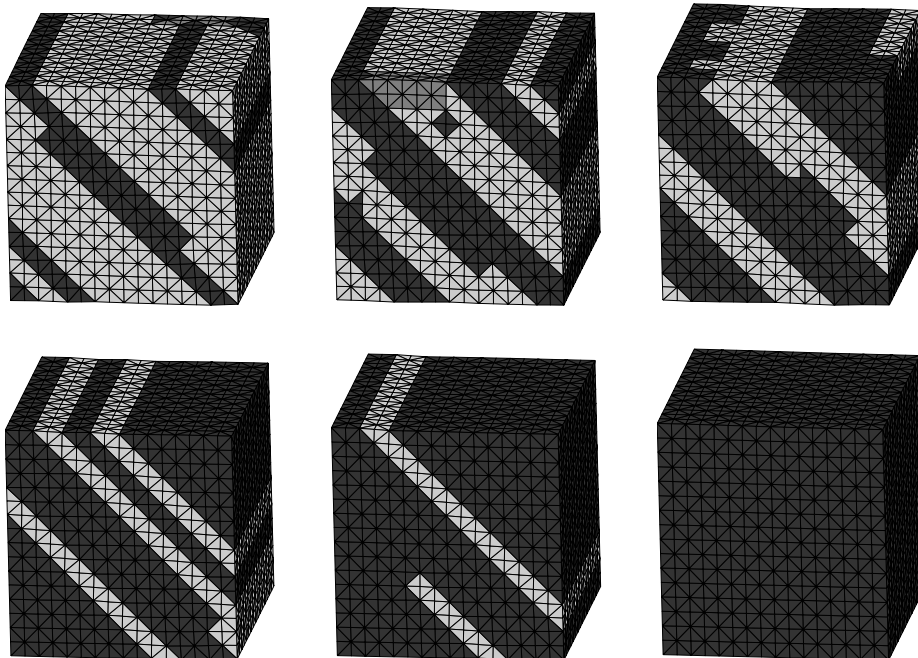


Fig. 6. Evolving microstructure in the simulation of the compression experiment at $T = 293$ K. The different gray shades indicate the different martensitic variants.

In Figure 6, some snapshots of the M/M phase transformation of the specimen in the compression simulation at 293 K are displayed, analogously to Figure 3 of the laboratory experiments. The front plane shows the [100] and [001] directions, the compression is applied in the horizontal direction. The different gray shades indicate the different martensitic variants. The austenitic phase does not occur in this experiment. One can clearly observe the same pattern of the laminated microstructure as in the laboratory experiment.

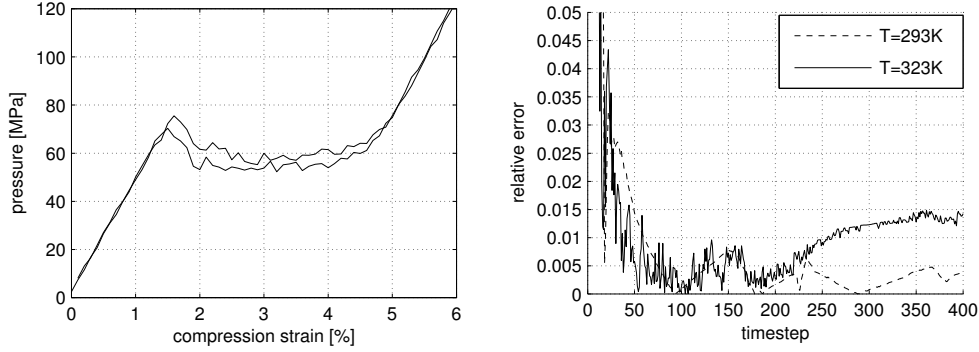


Fig. 7. Left: Stress-strain diagram for the numerical simulation without dissipation, $T = 323$ K. Right: Relative error in the energy balance, $T = 293$ K and $T = 323$ K.

For comparison reasons, we performed another compression simulation at $T = 323$ K for $\mathcal{E}_0 = \mathcal{E}_1 = 0$, i.e. when we switched the dissipative mechanism off. The resulting stress-strain diagram is given in the left part of Figure 7. The hysteresis loop in the transformation zone is very narrow compared to Figure 4. This shows that our algorithm does not produce any noteworthy numerical dissipation for the transformation from the austenitic phase to a single martensitic variant. Hence almost all dissipation in Figure 4 comes from the activated dissipative mechanism. Note however that the numerical algorithm produces a certain amount of numerical dissipation for the M/M transformation at $T = 293$ K which involves a complex fine-scale microstructure as in Figures 3 and 6.

Furthermore, we assured that the energy balance (28) derived in Section 2.3 is satisfied for the numerical simulations. A failing energy balance would indicate a high numerical dissipation or other undesired effects. The right graph of Figure 7 shows the relative error of the energy balance (28). Shortly after the beginning of the experiment with $T = 293$ K, it decreases to less than 0.2%. Even for the case $T = 323$ K, it stays well below 2%. This gives a-posteriori feedback information that the numerical errors are under control and that the optimization routine did not fail during the simulation process.

4 Conclusion

The stress-strain behavior of [001]-oriented NiMnGa single crystals in compression experiments was simulated. To this end, a continuum mechanical model was formulated which is based on a non-convex multiwell potential energy func-

tion and a plasticity-like rate-independent dissipative potential to deal with the mechanical hysteresis phenomenon. Numerical techniques were developed which allow the calculation of both the stress-strain constitutive response and the three-dimensional martensitic microstructure evolution with a reasonable accuracy. The simulation results were compared with the results of experimental compression tests at $T = 293$ K (twinning in martensite) and at $T = 323$ K (pseudoelasticity due to stress-induced martensitic transformation).

The results of the laboratory experiment and the computer simulation agree to a large extent, and the relevant physical phenomena of mechanical response and microstructure evolution are captured quite well. Furthermore our numerical methods are well capable to deal with the model.

Let us finally point out that the model and the numerical techniques can be used to simulate the mechanical response and the martensite microstructure evolution also in more complex deformation modes (for instance biaxial loading or twisting) where many other SMA models fail. Also, more complex geometries can be handled due to the flexibility of our finite element implementation.

Acknowledgements

M.A., M.G. and T.R. acknowledge the support from the University of Bonn and the “Sonderforschungsbereich 611”. T.R. acknowledges the support from the grants A 107 5402 (GA AV ČR) and MSM 0021620839 (MŠMT ČR). V.N., T.R. and P.Š. acknowledge the support from the grant MRTN-CT-2004-505226 “Multi-scale modelling and characterisation for phase transformations in advanced materials”.

References

- Abeyaratne, R., Knowles, J. K., 1992. On the propagation of maximally dissipative phase boundaries in solids. *Q. Appl. Math.* 50 (1), 149–172.
- Abeyaratne, R., Vedula, S., 1999. Propagation of a front by kink motion. In: Argoul, P., Frémond, M., Nguyen, Q. (Eds.), *IUTAM Symposium on Variations of Domains and Free-Boundary Problems in Solid Mechanics*. Kluwer, Dordrecht, pp. 77–84.
- Antman, S. S., 1998. Physically unacceptable viscous stresses. *Z. Angew. Math. Phys.* 49 (6), 980–988.
- Arndt, M., Griebel, M., 2005. Derivation of higher order gradient continuum models from atomistic models for crystalline solids. *Multiscale Model. Simul.* Accepted.
- Arndt, M., Griebel, M., Roubíček, T., 2003. Modelling and numerical simulation of martensitic transformation in shape memory alloys. *Contin. Mech. Thermodyn.* 15 (5), 463–485.
- Ball, J. M., James, R. D., 1987. Fine phase mixtures as minimizers of energy. *Arch. Ration. Mech. Anal.* 100, 13–52.
- Ball, J. M., James, R. D., 1992. Proposed experimental tests of a theory of fine microstructure and the two-well problem. *Philos. Trans. R. Soc. Lond. Ser. A* 338, 389–450.
- Bhattacharya, K., 1992. Self-accommodation in martensite. *Arch. Ration. Mech. Anal.* 120, 201–244.
- Bhattacharya, K., 2004. *Microstructure of Martensite. Why It Forms and How It Gives Rise to the Shape-Memory Effect*. Oxford University Press.

- Bhattacharya, K., Firoozye, N. B., James, R. D., Kohn, R. V., 1994. Restrictions on microstructure. *Proc. R. Soc. Edinb. Sect. A* 124 (5), 843–878.
- Ericksen, J. L., 1986. Constitutive theory for some constrained elastic crystals. *Int. J. Solids Struct.* 22 (9), 951–964.
- Ericksen, J. L., 1987. Some constrained elastic crystals. In: Ball, J. (Ed.), *Material Instabilities in Continuum Mechanics and Related Mathematical Problems*. Oxford University Press, pp. 119–137.
- Eve, R., Reddy, B., Rockafellar, R., 1990. An internal variable theory of elastoplasticity based on the maximum plastic work inequality. *Q. Appl. Math.* 48 (1), 59–83.
- Falk, F., 1980. Model free energy, mechanics and thermodynamics of shape memory alloys. *Acta Metallurgica* 28, 1773–1780.
- Falk, F., 1982. Landau theory and martensitic transitions. *J. Phys. C* 43 (12), 3–15.
- Falk, F., Konopka, P., 1990. Three-dimensional Landau theory describing the martensitic phase transformation of shape-memory alloys. *J. Phys. Cond. Matter* 2 (1), 61–77.
- Frémond, M., 1987. Matériaux à mémoire de forme. *C. R. Acad. Sci., Paris, Sér IIB* 304, 239–244.
- Frémond, M., Miyazaki, S., 1996. *Shape Memory Alloys*. CISM International Centre for Mechanical Sciences. Springer.
- Govindjee, S., Mielke, A., Hall, G. J., 2003. The free energy of mixing for n -variant martensitic phase transformations using quasi-convex analysis. *J. Mech. Phys. Solids* 51 (4), I–XXVI.
- Hill, R., 1948. A variational principle of maximum plastic work in classical plasticity. *Q. J. Mech. Appl. Math.* 1, 18–28.
- James, R. D., 1996. Hysteresis in phase transformations. In: Kirchgässner, K., Mahrenholtz, O., Mennicken, R. (Eds.), *Proceedings ICIAM 95*. Vol. 87 of *Mathematical Research*. Akademie Verlag, Berlin, pp. 135–154.
- James, R. D., Hane, K. F., 2000. Martensitic transformations and shape-memory materials. *Acta Mater.* 48 (1), 197–222.
- Karaca, H. E., Karaman, I., Lagoudas, D. C., Maier, H. J., Chumlyakov, Y. I., 2003. Recoverable stress-induced martensitic transformation in a ferromagnetic CoAlNi alloy. *Scripta Mater.* 49, 831–836.
- Klouček, P., Luskin, M., 1994. The computation of the dynamics of the martensitic transformation. *Contin. Mech. Thermodyn.* 6 (3), 209–240.
- Kružík, M., Otto, F., 2004. A phenomenological model for hysteresis in polycrystalline shape memory alloys. *Z. Angew. Math. Mech.* 84 (12), 835–842.
- Kružík, M., Roubíček, T., 2004. Mesoscopic model of microstructure evolution in shape memory alloys with applications to NiMnGa. Preprint No. 2003, IMA, University of Minnesota.
- Leclerq, S., Bourbon, G., Lexcellent, C., 1995. Plasticity like model of martensite phase transition in shape memory alloys. *J. Phys. IV* 5, 513–518.
- Luskin, M., 1996. On the computation of crystalline microstructure. *Acta Numer.* 5, 191–257.
- Mañosa, L., González-Comas, A., Obradó, E., Planes, A., Chernenko, V. A., Kokorin, V. V., Cesari, E., 1997. Anomalies related to the TA_2 -phonon-mode condensation in the Heusler Ni₂MnGa alloy. *Phys. Rev. B* 55 (17), 11068–11071.
- Mielke, A., Roubíček, T., 2003. A rate-independent model for inelastic behavior of shape-memory alloys. *Multiscale Model. Simul.* 1 (4), 571–597.

- Mielke, A., Theil, F., 1999. Mathematical model for rate-independent phase transformations with hysteresis. In: Alber, H.-D., Baean, R., Farwig, R. (Eds.), *Models of Continuum Mechanics in Analysis and Engineering*. Shaker-Verlag, Aachen, pp. 117–129.
- Mielke, A., Theil, F., Levitas, V. I., 2002. A variational formulation of rate-independent phase transformations using an extremum principle. *Arch. Ration. Mech. Anal.* 162 (2), 137–177.
- Müller, S., 1999. Variational models for microstructure and phase transitions. In: Hildebrandt, S., Struwe, M. (Eds.), *Calculus of Variations and Geometric Evolution Problems*. Vol. 1713 of *Lecture Notes in Mathematics*. Springer, pp. 85–210.
- Pitteri, M., Zanzotto, G., 2002. *Continuum Models for Phase Transitions and Twinning in Crystals*. Chapman & Hall/CRC Press, Boca Raton.
- Plecháč, P., Roubíček, T., 2002. Visco-elasto-plastic model for martensitic phase transformation in shape-memory alloys. *Math. Methods Appl. Sci.* 25 (15), 1281–1298.
- Rajagopal, K. R., Roubíček, T., 2003. On the effect of dissipation in shape-memory alloys. *Nonlinear Anal. Real World Appl.* 4 (4), 581–597.
- Rajagopal, K. R., Srinivasa, A. R., 1998. On the inelastic behaviour of solids — part 1, twinning. *Int. J. Plast.* 11 (6), 653–678.
- Raniecki, B., Lexcelent, C., Tanaka, K., 1992. Thermodynamic models of pseudoelastic behavior of shape memory alloys. *Arch. Mech.* 44 (3), 261–284.
- Ren, X., Truskinovsky, L., 2000. Finite scale microstructures in nonlocal elasticity. *J. Elasticity* 59 (1-3), 319–355.
- Rogers, R. C., Truskinovsky, L., 1997. Discretization and hysteresis. *Physica B* 233 (4), 370–375.
- Roubíček, T., 2000. Dissipative evolution of microstructure in shape memory alloys. In: Bungartz, H.-J., Hoppe, R. H. W., Zenger, C. (Eds.), *Lectures on Applied Mathematics*. Springer, Berlin, pp. 45–63.
- Roubíček, T., 2004. Models of microstructure evolution in shape memory alloys. In: Ponte Castaneda, P., Telega, J. J., Gambin, B. (Eds.), *Nonlinear Homogenization and its Applications to Composites, Polycrystals and Smart Materials*. Vol. 170 of *NATO Science Series II: Mathematics, Physics and Chemistry*. Kluwer, Dordrecht, pp. 269–304.
- Roubíček, T., Kružík, M., 2005. Mesoscopic model of microstructure evolution in shape memory alloys, its numerical analysis and computer implementation. In: Miehe, C. (Ed.), *3rd GAMM Seminar on microstructures*. *GAMM Mitteilungen*. J. Wiley, to appear.
- Salamon, P., Sibani, P., Frost, R., 2002. *Facts, Conjectures, and Improvements for Simulated Annealing*. Vol. 7 of *Monographs on Mathematical Modeling and Computation*. SIAM, Philadelphia.
- Sozinov, A., Likhachev, A. A., Lanska, N., Söderberg, O., Koho, K., Ullakko, K., Lindroos, V. K., 2004. Stress-induced variant rearrangement in Ni-Mn-Ga single crystals with nonlayered tetragonal martensitic structure. *J. Phys. IV* 115 (3), 121–128.
- Straka, L., Novák, V., Landa, M., Heczko, O., 2004. Acoustic emission of Ni-Mn-Ga magnetic shape memory alloy in different straining modes. *Mater. Sci. Eng. A* 374 (1-2), 263–269.
- Truskinovsky, L., 1994. Transition to detonation in dynamic phase changes. *Arch. Ration. Mech. Anal.* 125 (4), 375–397.
- Truskinovsky, L., Vainchtein, A., 2004. The origin of nucleation peak in transformational plasticity. *J. Mech. Phys. Solids* 52 (6), 1421–1446.

Bestellungen nimmt entgegen:

Institut für Angewandte Mathematik
der Universität Bonn
Sonderforschungsbereich 611
Wegelerstr. 6
D - 53115 Bonn

Telefon: 0228/73 3411

Telefax: 0228/73 7864

E-mail: anke@iam.uni-bonn.de

Homepage: <http://www.iam.uni-bonn.de/sfb611/>

Verzeichnis der erschienenen Preprints ab No. 200

200. Albeverio, Sergio; Ayupov, Shavkat A.; Omirov, Bakhrom A.: Cartan Subalgebras and Criterion of Solvability of Finite Dimensional Leibniz Algebras; eingereicht bei: Journal of Lie Theory
201. not published
202. Sturm, Karl-Theodor: Convex Functionals of Probability Measures and Nonlinear Diffusions on Manifolds; erscheint in: J. Math. Pures Appl.
203. Sturm, Karl-Theodor: On the Geometry of Metric Measure Spaces
204. Müller, Jörn; Müller, Werner: Regularized Determinants of Laplace Type Operators, Analytic Surgery and Relative Determinants
205. Mandrekar, Vidyadhar; Rüdiger, Barbara: Lévy Noises and Stochastic Integrals on Banach Spaces
206. Albeverio, Sergio; Proskurin, Daniil; Turowska, Lyudmila: On $*$ -Representations of the λ -Deformation of a Wick Analogue of the CAR Algebra
207. Albeverio, Sergio; Fei, Shao-Ming; Song, Tong-Qiang: Multipartite Entangled State Representation and its Squeezing Transformation
208. Albeverio, Sergio; Pratsiovytyi, Mykola; Torbin, Grygoriy: Topological and Fractal Properties of Real Numbers which are not Normal; eingereicht bei: Bull. Sci. Math.
209. Albeverio, Sergio; Cattaneo, Laura; Fei, Shao-Ming; Wang, Xiao-Hong: Multipartite States Under Local Unitary Transformations
210. Albeverio, Sergio; Bozhok, Roman; Dudkin, Mykola; Koshmanenko, Volodymyr: Dense Subspaces in Scales of Hilbert Spaces
211. Otto, Felix; Westdickenberg, Michael: Eulerian Calculus for the Contraction in the Wasserstein Distance; eingereicht bei: SIAM J. Math. Anal.
212. Albeverio, Sergio; Smorodina, Nataliya V.: The Multiple Stochastic Integrals and the Transformations of the Poisson Measure
213. Albeverio, Sergio; Pustyl'nikov, Lev D.: Some Properties of Dirichlet L -Functions Associated with their Nontrivial Zeros I.

214. Ebmeyer, Carsten: Regularity in Sobolev Spaces for the Fast Diffusion and the Porous Medium Equation; erscheint in: J. Math. Anal. Appl.
215. Albeverio, Sergio; Korolyuk, Volodymyr S.; Bratiychuk, Mykola S.: Asymptotic Behaviour of the Ruin Probability for Stochastic Risk Models
216. Albeverio, Sergio; Korolyuk, Volodymyr S.; Lebedev, E.A.; Chechelnitsky, A.A.: Functional Limit Theorems for Multi-Channel Networks
217. Albeverio, Sergio; Binding, Paul; Hryniv, Rostyslav; Mykytyuk, Yaroslav: Inverse Spectral Problems for Coupled Oscillating Systems
218. Kornhuber, Ralf; Krause, Rolf: Robust Multigrid Methods for Vector-Valued Allen-Cahn Equations with Logarithmic Free Energy
219. Albeverio, Sergio; Konstantinov, Alexei; Koshmanenko, Volodymyr: Remarks on the Inverse Spectral Theory for Singularly Perturbed Operators
220. Otto, Felix; Rump, Tobias; Slepčev, Dejan: Coarsening Rates for a Droplet Model: Rigorous Upper Bounds
221. Gozzi, Fausto; Marinelli, Carlo: Stochastic Optimal Control of Delay Equations Arising in Advertising Models
222. Griebel, Michael; Oeltz, Daniel; Vassilevsky, Panayot: Space-Time Approximation with Sparse Grids
223. Arndt, Marcel; Griebel, Michael; Novák, Václav; Šittner, Petr; Roubíček, Tomáš: Martensitic Transformation in NiMnGa Single Crystals: Numerical Simulation and Experiments